CHAPTER

11 Observing Frontal Instabilities of the Florida Current Using High Frequency Radar

Matthew R. Archer*, **Lynn K. Shay**, **Benjamin Jaimes**, **Jorge Martinez-Pedraja**

Department of Ocean Sciences, Rosenstiel School of Marine and Atmospheric Science, University of Miami, FL, USA

**Corresponding author: E-mail: matthew.robert.archer@gmail.com*

CHAPTER OUTLINE

Coastal Ocean Observing Systems. http://dx.doi.org/10.1016/B978-0-12-802022-7.00011-0

1. INTRODUCTION

The Florida Current (FC) is a western boundary current regime characterized by large velocities, strong horizontal shears, and relative vorticities that can approach $10f$, where f is the local Coriolis parameter.[1] This current is constrained in close proximity to the coastline by the narrow Straits of Florida (SOF) channel, which guides it from the Gulf of Mexico to the South Atlantic Bight. It is one of the most studied ocean currents in the world because of its importance in the meridional transport of heat from the tropics to the poles, its proximity to the United States coastline, and the experimental convenience of the channel-like bathymetry within the SOF. The mean structure, volume transport, and low-frequency variability of the FC have been examined in detail by numerous studies (e.g., Refs. 2—7). Instabilities along the frontal region of the FC have been observed and modeled.[1,8—14] However, there are still many gaps in our understanding. Questions are now directed at the dynamics of the smaller scale shear-zone instabilities, especially on the eastern front of the FC, which has not yet been addressed because of lack of observations.

Research aimed at understanding the coastal ocean circulation in the SOF is extremely valuable to policymakers who must balance societal interests and environmental concerns. Improving our capability to measure and predict the ocean currents will benefit a broad spectrum of societally relevant applications: search and rescue (SAR), maritime security, navigation, fisheries management, commercial shipping interests, and oil spill mitigation. However, near coastal ocean processes are difficult to study because of the variability in the forcing mechanisms that occur over a wide range of temporal and spatial scales. In the coastal SOF, the primary forcing is from the meandering FC and the wind, but the ocean response is complicated by the geometry of the coastline and underlying bathymetry. The effect of stratification (e.g., buoyant riverine output) and tidal currents also influence the circulation pattern inshore.

Previous research in the FC has been largely lead by in situ measurements, such as hydrographic sections or moorings, which have provided reasonable coverage in space or time, but not both. Traditional in situ instruments and satellites do not as easily observe flow features with smaller horizontal scales (the submesoscale) that evolve more quickly in time (on the order of hours). HF radar can provide two-dimensional maps of coastal ocean surface currents in near real time, with the ability to sample at intervals as little as a few minutes and a spatial resolution of less than a kilometer. This allows us to resolve small-scale flow features at the surface within the SOF.

This chapter documents new observations of frontal instabilities of the FC using HF radar. Two case studies demonstrate the power of HF radar for coastal ocean observing. In the first case, a study of a submesoscale frontal eddy in the cyclonic shear-zone of the FC is presented. The emphasis is on the ability of HF radar to provide new insight into spatial variability of these features, using the two-dimensional velocity field and its derivatives to investigate their kinematics. Understanding the flow field provides insight into particle dispersion, which if known could help in SAR operations and pollution mitigation. These eddies also contribute to cross-shelf exchange of mass and nutrients, which has implications for biological productivity along the Florida Keys and South Florida coastlines.[15]

In the second case study, a near-inertial signal in the eastern anticyclonic flank of the FC is presented for the first time. This is an example of HF radar's unique ability to measure transient events that are difficult to capture with ship and in situ point measurements, or to resolve using satellite imagery. These features could have implications for mixing and cross-shelf exchange on the eastern side of the channel.

A background review of the scales of variability of the FC, together with a discussion of open questions, is provided in Section 2. Instrumentation is described in Section 3. The two case studies are presented in Sections 4 and 5 of cyclonic and anticyclonic shear-zone instability, respectively. Finally, the results are summarized and the direction for future work is discussed.

2. BACKGROUND: THE FLORIDA CURRENT

2.1 INSTABILITY OF THE FLORIDA CURRENT

The FC transports warmer water of equatorial origin northward through cooler local waters. This results in two frontal regions on either side of the jet core, which are narrow zones of enhanced horizontal gradients of velocity and temperature. These high-shear frontal regions are subject to instabilities that can result in mixing of the water masses. Such instabilities are an important link between littoral and offshore waters as they can act to redistribute heat, salt, momentum, and nutrients. For example, cyclonic eddies have been shown to play a significant role in larval recruitment along the Florida Keys reef tract, where upwelling in the eddy core produces favorable conditions during the early stages of development.[15,16]

A summary of the time and space scales of the instabilities in the SOF, based on observations published in the literature, is presented in Figure 1. It reveals a broad spectrum of scales, ranging from slower, larger meanders and Tortugas eddies to smaller, rapidly evolving features such as submesoscale vortices and a super-tidal oscillation. These features are not independent but are strongly influenced by one another and the dynamics of the FC.

2.2 MEANDERING

Meanders are characterized by a lateral wave-like movement of the FC axis. These waves are asymmetric, with the crests (shoreward displacement) and troughs

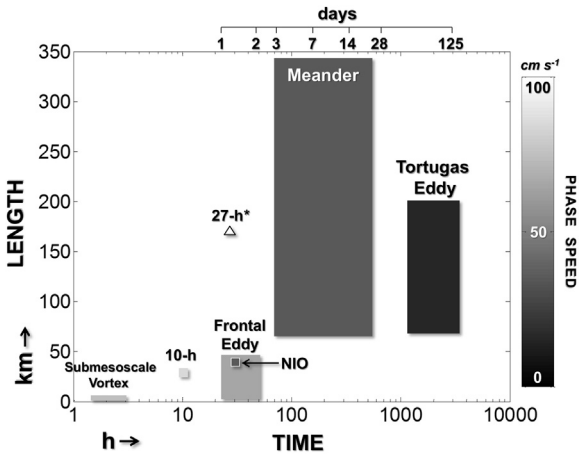

FIGURE 1

The scales of time, length, and phase speed of the instabilities that have been observed in the Straits of Florida. *The 27-h signal phase speed observed by Peters et al.[1] is 170 cm/s.

Refs 1,5,8–11,13–15,19–21,23–27.

(offshore displacement) leading on the eastern side of the channel.[5,17] These unstable barotropic modes can be forced by small perturbations in regions of high horizontal shear.[8] Their wavelengths range from 70 km to a few hundred kilometers, with periods of several days to weeks. In the meridional SOF, the most energetic meandering signals are centered at 5 and 12 days, with phase speeds (wavelengths) of 40 cm/s (170 km) and 25 cm/s (340 km).[5] Cross-channel amplitudes decrease from $\mathcal{O}$ (100 km) in the western entrance to $\mathcal{O}$ (10 km) offshore of Miami because of the narrowing channel and shoaling topography.[18]

2.3 CYCLONIC EDDIES

Associated with the meander troughs are cyclonic eddies that are advected downstream in between the Florida coastline and the FC. Quasi-stationary mesoscale "Tortugas" eddies (100−200 km diameter) are observed in the southern SOF off the Dry Tortugas.[9,19] Their generation mechanism is connected to an extreme southward orientated Loop Current (LC) as it enters the straits, and their subsequent advection is forced by approaching upstream LC frontal eddies. Smaller scale (10−50 km) frontal eddies (also termed spin-off eddies, or edge-eddies) have been measured throughout the year over different bathymetric features along the SOF.[8,14,20,21] They are not directly related to wind forcing, although strong wind events perturb the high-shear regime that may lead to FC instabilities and eddy generation.[8] The lifespan of frontal eddies is estimated to be between one to three weeks, with an average one week occurrence.[8] The passage of these eddies distorts

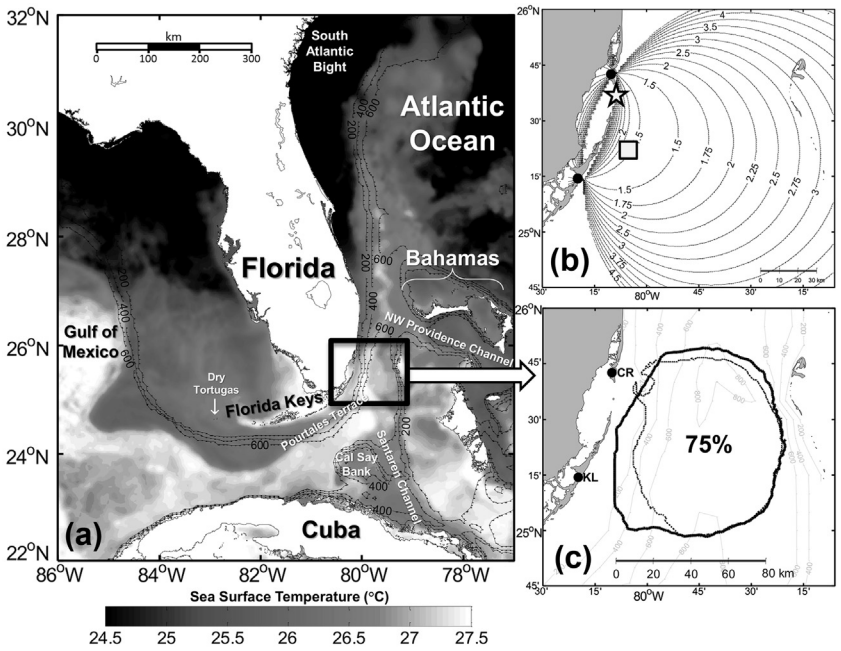

FIGURE 2

(a) 1-day mean SST from MODIS at 1-km resolution for May 7, 2006 (http://mur.jpl.nasa.gov/). Depth contours in meters. (b) Geometric Dilution of Precision (GDOP; see Section 3 for a definition). Star: Fowey Rocks C-MAN station. Square: Acoustic Doppler Current Profiler used in comparison by Parks et al.[14] (c) The 75% radar data coverage contour during the cyclonic case study (dashed line) and the anticyclonic case study (solid line). Black circles pinpoint radar site locations at Crandon Park (CR) and Key Largo (KL).

the thermal structure over the shelf break, which is visible in satellite sea surface temperature (SST) imagery (Figure 2(a)). Uplifted isotherms associated with the cyclonic circulation create a cool surface band of water near the center of the vortex. This produces a strong SST signature characterized by a warm tongue-like extrusion forced by the southward-oriented currents, with a cold upwelling region between the FC and the extruding filament that has an isopycnal uplift of approximately 10 m per day in the upper 200 m.[8] In this sense, they are more akin to roll-vortices produced by wavelike rolling up of the shear-zone than isolated rings observed in the Gulf Stream after it detaches from the coastline.[22]

2.4 INTERNAL WAVES

A complex internal wave (IW) field is created by the strongly sheared current velocity regime and narrow channel with steep topographic gradients.[28] IWs contribute to the generation and distribution of turbulent mixing and mass transfer

to coral reef communities along the Keys.[29] Sources of IW energy are the interaction of the barotropic (surface) tide with the along-shelf topography and FC fluctuations.[13,26] The IW field is particularly energetic in the spring and summer months (March–October) because of the uplift of the pycnoclines on the western side of the SOF.[30] Propagation of frontal eddies along the Florida Keys reef tract has been associated with enhanced high frequency IW energy and a peak of diurnal-band spectral power in near shore barotropic currents.[16,26]

2.5 HF RADAR OBSERVATIONS OF FC INSTABILITIES

Since the mid-1990s the deployment of HF radar systems along the South Florida coastline has provided a unique opportunity to investigate the spatial variability of ocean surface currents within the SOF (e.g., Refs. 1,10,11,14). Several frontal eddies have been observed and described, along with new velocity signals. The findings are summarized below.

Two cyclonic frontal eddies were mapped by Haus et al.[21] seaward of Hawk Channel off Key Largo. They occurred when the FC axis was further offshore, with large frontal shears because of wind-forced southwestward inner-shelf currents. Both eddies were elongated in the along-shore direction (19 by 15 km and 47 by 25 km) with fast downstream translation speeds (53 cm/s and 80 cm/s). Parks et al.[14] described a cyclonic submesoscale eddy offshore of Miami with a diameter of approximately 15 km and moving at 45 cm/s. A moored acoustic Doppler current profiler (ADCP) revealed it had a barotropic structure, characterized by a westward u-component through the entire water column over a 48-h period.

A near-inertial oscillation translating eastward along the 150-m isobath off Key West was observed by Shay et al.[10] The signal moved along the inshore edge of the FC at 30 cm/s, exhibiting a dipole-like structure of the current vectors in space. The signal was embedded in the near-inertial passband and absent in the subinertial band. They suggest it was forced by an abrupt change in wind stress, consistent with analytical model results of Kundu.[31] The FC jet trapped the higher frequency near-inertial motions because of negative vorticity, and it amplified these motions in the positive vorticity (cross-shelf gradient $\pm 2f$) regime.

Shay et al.[11] utilized very high frequency (VHF) radar with a horizontal resolution of 250 m. Several submesoscale vortices were observed with diameters of 2 to 3 km over the shelf break at Ft Lauderdale. The translation speed of these features was approximately 30 cm/s, consistent with that of frontal eddies and near-inertial motions; although these vortices are an order of magnitude smaller. They concluded that the vortex they investigated was linked to FC intrusions over the shelf break because it occurred during a period of weak wind conditions.

Two dominant modes of narrowband frequency embedded in the subinertial FC flow were investigated by Peters et al.[1]: a 10-h (super-tidal) signal with amplitude near 50 cm/s and an equally strong 27-h signal (close to the local inertial period). Both signals appeared barotropic in shallow water (50 m depth), but farther offshore

(160 m depth), the 10-h signal exhibited baroclinicity with a phase reversal at depth. The 10-h signal "leaned against the shear" (phase trend in the east−west direction), which is consistent with unstable, growing waves that draw energy from the mean flow. Neither signal could be associated with mesoscale meandering or the near-inertial broadband oscillation observed by Shay et al.[10]

2.6 WIND FORCING

The wind field in the SOF is dominated by the easterly trade wind regime, with a significant northeasterly component during the wintertime.[32] From October to March, cold frontal passages provide forcing with a period range of 4 to 12 days. In summer, the disturbances are due to tropical and subtropical depressions with periods from 15 to 30 days.[33] Strong fluctuations in along-channel wind stress produce a high correlation with measured large-scale transport variations, which vary by time scale depending on the season.[33] Observed frontal instabilities may be a result of wind stress forcing on the shear region of the FC; however, wind does not appear to be a controlling forcing mechanism because these instabilities are prevalent across all seasons.[8]

2.7 OPEN SCIENTIFIC QUESTIONS

In a numerical study of the Gulf Stream along the South Atlantic Bight, Xue and Bane[34] investigated frontal instabilities on either side of the jet core. They note clockwise rotation on the offshore side of the meander crests. Fiechter and Mooers[12] modeled FC instabilities, and though their focus was on cyclonic eddies (like all studies in the SOF), they noted the presence of frontal instabilities in the eastern shear-zone.

Observations from moored current meters through the SOF have hinted at anticyclonic shear-zone instabilities.[2,19] When the FC is in an offshore meander over the Pourtales Terrace, it interacts with the Cal Say Bank.[2] Lee et al.,[19] using SST imagery, observed an offshore FC meander that was partially diverted clockwise around the Cal Say Bank and into the Santaren Channel, which set up a cyclonic rotation. These results suggest that eddies could be formed upstream because of instability of the meandering FC impinging on the steep shelf break of the Cal Say Bank. This interaction may form either anticyclonic (directly) or cyclonic (indirectly through the Santaren Channel) circulations. Another mechanism could be wind stress perturbations on the laterally sheared jet, which because of its unstable nature can encourage fast-growing modes.[8]

Anticyclonic shear-zone instabilities in the SOF have not received attention in the research literature, thus very little is known about their kinematics or dynamics. In this study, HF radar will be used to investigate the spatial and temporal characteristics of an anticyclonic instability, to begin to elucidate the kinematics of these features.

3. INSTRUMENTATION AND EXPERIMENTAL DESIGN

3.1 HF RADAR—PRINCIPLES OF OPERATION

The basic physics of backscattering of electromagnetic waves from the sea surface was identified by Crombie,[35] who observed that the sea echo spectra showed a slight Doppler shift from the transmitted signal. The Doppler shift is the change in frequency (and wavelength) emitted or reflected by an object because of motion. Surface waves with one-half of the incident wavelength produce an enhanced backscatter phenomenon known as resonant Bragg scattering. Bragg scattering results in two distinct peaks in the Doppler spectrum, shifted from the transmit frequency by an amount proportional to the deep water phase speed of the Bragg waves based on linear wave theory. The Doppler frequency shift can be calculated as follows:

$$f_B = \pm \sqrt{\frac{g f_R}{\pi c}} \tag{1}$$

where g is acceleration because of gravity, f_R is the radar transmit frequency, and c is the speed of light. The presence of an underlying surface current will further shift the Bragg peaks by an amount Δf:

$$\Delta f = \frac{2 V_r f_R}{c} \tag{2}$$

where V_r is the radial current along the look direction of the radar. By measuring Δf, V_r can be calculated. At least two radar sites are required to resolve vector current velocities from radial measurements.

The effective centroid depth of the measurement depends on the depth of influence of the Bragg waves, shown by Stewart and Joy[36] to be $d = \lambda/8\pi$ (λ is the transmit wavelength). Stable estimates require scattering from hundreds of wave crests plus ensemble averaging of the spectral returns, which sets the time−space resolution limits of the instruments.

3.2 EXPERIMENTAL DEPLOYMENT

Two WERA (Wellen Radar) systems were deployed from June 2004 to July 2011 at Crandon Park on Key Biscayne (CR, 25°42.84′N, 80°9.06′W) and north Key Largo (KL, 25°14.46′N, 80°18.48′W) in South Florida (Figure 2). The WERA systems were chosen for operational flexibility; the user sets the parameters that determine the desired capabilities for the experiment (see Table 1). These WERAs operate in beamforming mode, where a narrow beam is electronically steered over the illuminated ocean, attaining more accurate data returns.[37] Each site operates at 16.045 MHz, obtaining data on a radial grid with resolution of 1.2 km range and 7.5° azimuth, every 20 min, out to approximately 80 km.

Conversion from a radial grid (range and azimuth) to a 1.2 km resolution Cartesian grid is performed on the Doppler spectra. For a given Cartesian grid point, the four closest spectra are identified, two in range and two in azimuth. These four spectra, weighted by distance, are interpolated onto the Cartesian grid point (Klaus-Werner

Table 1 Parameters and Capabilities of the WERA System Operating at 16.045 MHz

Parameters	Value	Capabilities	Value
Operating frequency (MHz)	16.045	Average range (km)	80
Transmit wavelength (m)	18.7	Range cell resolution (km)	1.2
Bragg wavelength (m)	9.35	Measurement depth (m)	0.75
Bragg deep water phase speed (cm/s)	38	Sampling interval (min)	4.5
Bragg frequency shift (Hz)	0.408	Azimuth resolution (°)	7.5
Chirp length (#)	1024		
Chirp duration (s)	0.26		
Modulation bandwidth (KHz)	125		
Transmit elements (square array) (#)	4		
Receive elements (#)	16		
Transmitter peak power (W)	30		

Gurgel, personal communication). Radial velocities are calculated from interpolated spectra every 20 min using manufacturer supplied software. Vectors are calculated every 10 min, using the alternating 20 min radial measurements, with an unweighted least squares method.[38] Velocity field derivatives are calculated using centered differencing.[39] Vector current accuracy is a function of the angle of intersection between the radials from each site, termed the geometric dilution of precision (GDOP), and it can be thought of as a multiplier of the measurement noise.[40] The GDOP ranges from 1 to 2.5 in the radar domain (Figure 2(b)). For this analysis, computed current vectors were filtered with a 7-point Hanning window in time at each grid point. Data points over 3 standard deviations (STD) from a 5 day running mean, and grid points that exceeded a threshold STD of 40 cm/s, or with less than 25% data coverage, were removed from the analysis (see Figure 2(c) for spatial coverage). Comparison with an acoustic Doppler current profiler (location in Figure 2(b)) at the 14 m bin depth revealed root mean square differences between 10 and 30 cm/s.[14]

4. CYCLONIC SHEAR-ZONE INSTABILITY

4.1 OBSERVED SURFACE CURRENT FIELD

A cyclonic frontal eddy was observed translating downstream, inshore of the FC, from 18 to 21 January, 2005 (Figure 3). The eddy was almost stationary in the southernmost part of the domain for ~48 h. Then on 20 January at approximately 12:00 (all times in UTC), it began propagating northward along the 200 m isobath, over a 36-h period. During the passage, downstream current velocities in the FC approached 200 cm/s, and the southward tangential flow of the eddy reached 80 cm/s. The eddy was nestled in the trough of an FC meander, which translated with the feature.

The length scale of the eddy was approximately 20 km. This value is estimated based on the tangential velocities not contaminated by the strong mean flow. As the

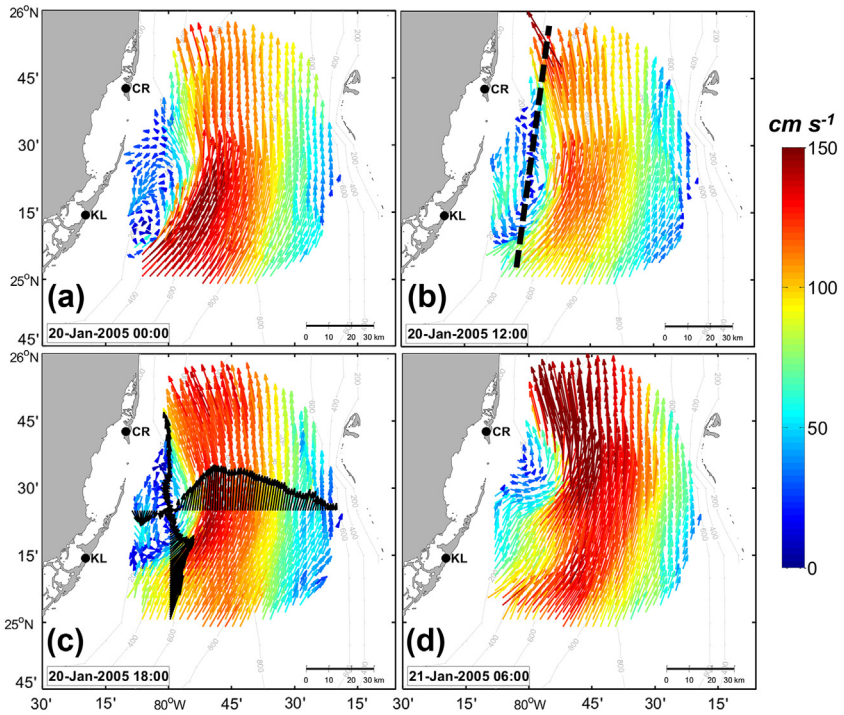

FIGURE 3

Four snapshots of surface current vectors (hourly averaged) at (a) 20 Jan 00:00 UTC, (b) 20 Jan 12:00 UTC, (c) 20 Jan 18:00 UTC and (d) 21 Jan 06:00 UTC depict a submesoscale frontal eddy, which propagates northward along the inshore edge of the Florida Current. Dashed line in (b) depicts transect used for Hovmöller (Figure 4), and the black velocity vectors in (c) highlight the radial horizontal profile of the eddy and the FC.

eddy translated downstream, it moved inshore, and thus, its shoreward side gradually exited the HF radar footprint. The length scale is near the first baroclinic mode Rossby radius of deformation, which has been measured to be between 15 and 30 km in the SOF.[1,11] The eddy is defined as submesoscale, based on its $\mathcal{O}(1)$ Rossby number (see later discussion). The signal propagated north at ~46 km per day (53 cm/s), measured using the slope (Δ *latitude*/Δ *time*) of the *u*-component (Figure 4).

Associated with the passage of this frontal eddy was a strong SST front along the western wall of the FC (Figure 5). The 1 day mean cross-frontal SST gradient was 0.9°C/km on 20 January, compared to 0.04°C/km along the anticyclonic front east of the FC core, and 0.02°C/km at the cyclonic front at a latitude outside the feature (Figure 5(d)). A map of the 1 day mean surface current velocity field superimposed on the SST image reveals the warm FC meander, and within its trough the cold frontal eddy. The translating feature has been smeared by the 1 day average, but there is a correlation between the vectors and SST gradients. Warmer water surrounds a

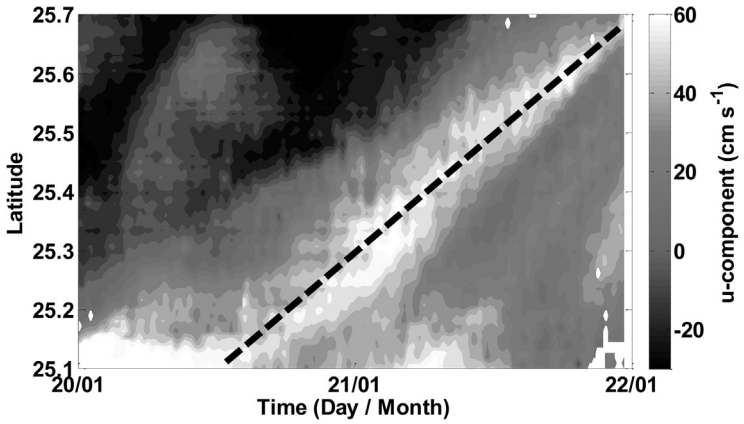

FIGURE 4

Hovmöller diagram of the *u*-component of velocity (cm/s) as a function of latitude (*y*-axis) and time in day/month (*x*-axis). Black dashed line indicates the slope (= speed) of the signal propagation: 66 km/34 h = 46 km per day, or 53 cm/s. The transect follows the path of the eddy, shown in Figure 3(b).

core of cooler water, presumably upwelled because of divergence at the surface since horizontal temperature advection is unlikely considering the temperature of the ambient surface water. The cross-frontal structure at the latitude of the eddy's core is shown in Figure 5(b)–(d). The flow is cyclonic and divergent to the west of the jet core, and maximum values correspond to the FC front where the gradient in the velocity is greatest.

Pressure charts (not shown) indicate the progression of a cold front that passed the SOF on 15 January. A southward wind approached 10 m/s on 17 January with wind stress (surface frictional velocity) over 50 cm/s,[14] which forced a southward countercurrent. As the cold front moved through, the wind weakened and shifted to the southwest on 20 January. At this time, the eddy began propagating north.

4.2 FLOW FIELD KINEMATICS

The dispersion of passive tracers, such as phytoplankton or oil, is primarily controlled by ocean currents and wind. Understanding transport of passive tracers on the ocean surface has practical application, most notably for SAR operations and oil spill mitigation. Disregarding the effects of wind and unresolved small-scale processes, passive tracer (or particle) dispersion is a function of the velocity gradient tensor, the components of which can be calculated with the HF radar dataset. It is of interest to compare how the flow field kinematics change between an eddy event (e.g., a frontal eddy) and normal background conditions.

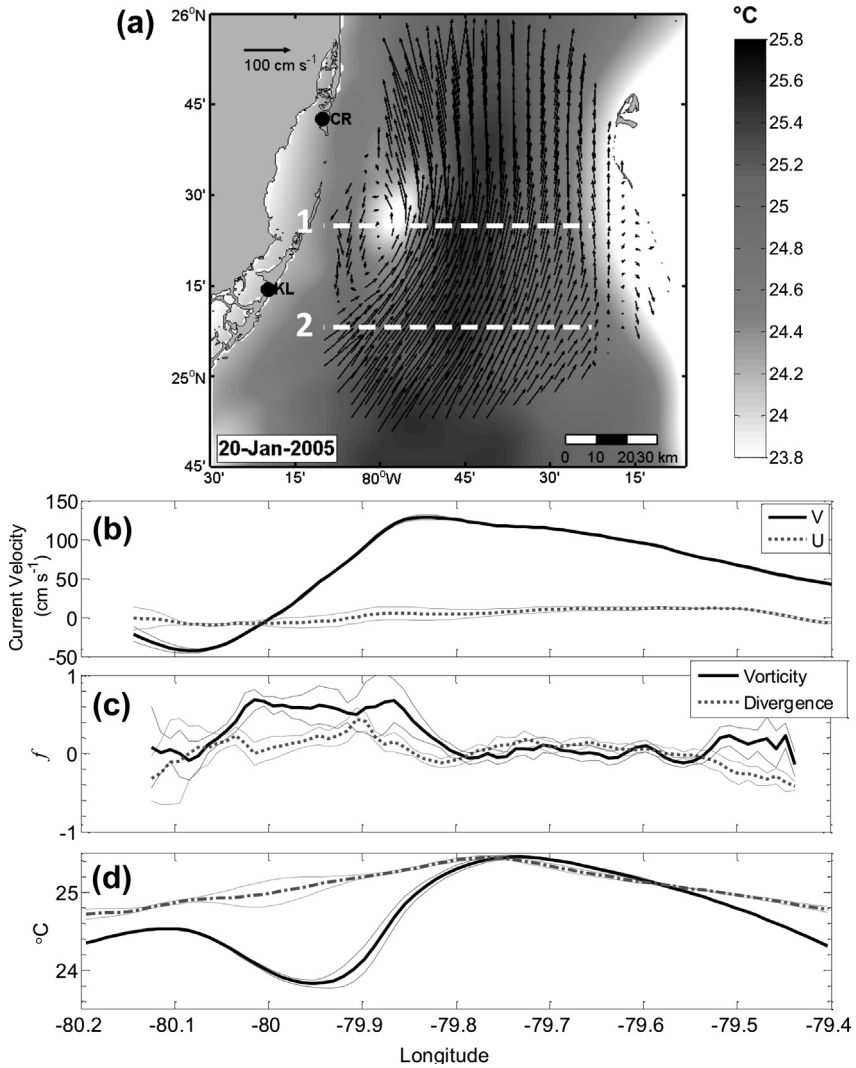

FIGURE 5

(a) 1 day mean SST (°C) from MODIS at 1 km resolution (http://mur.jpl.nasa.gov/). Superimposed on this is the 1 day mean HF radar–derived surface current field, which reveals upwelling in the core of the cyclonic submesoscale eddy. White dotted lines 1 and 2 denote the latitude of the cross-sections plotted below. (b) Cross-section of *u*- and *v*-component of velocity along line 1, (c) vorticity and divergence normalized by local Coriolis frequency along line 1, and (d) SST along line 1 (solid line) and line 2 (dot-dashed line). Thin dotted lines indicate the standard deviation over 25.34–25.47°N (line 1) and 25.09–25.20°N (line 2).

4.3 VELOCITY GRADIENT TENSOR

A two-dimensional surface velocity field, $\boldsymbol{u}(\boldsymbol{x},t) = (u(x,y,t),v(x,y,t))$, can be expanded into a Taylor's series near a reference point x_0.[41] Discarding higher order terms gives the following:

$$\boldsymbol{u}(\boldsymbol{x},t) = \boldsymbol{u}_0 + \boldsymbol{a}\,(x(t) - x_0(t)) \tag{3}$$

where $\boldsymbol{u}_0 = \boldsymbol{u}(\boldsymbol{x}_0)$ is the mean velocity and $\boldsymbol{a}$ is the second-order velocity gradient tensor:

$$\boldsymbol{a}_{ij} \equiv \nabla u = \begin{bmatrix} \dfrac{\partial u}{\partial x} & \dfrac{\partial u}{\partial y} \\ \dfrac{\partial v}{\partial x} & \dfrac{\partial v}{\partial y} \end{bmatrix} \tag{4}$$

The following elemental components may be defined:[42]

$$\text{vorticity} \quad \frac{\partial v}{\partial x} - \frac{\partial u}{\partial y} \equiv \zeta \tag{5}$$

$$\text{divergence} \quad \frac{\partial u}{\partial x} + \frac{\partial v}{\partial y} \equiv d \tag{6}$$

$$\text{normal strain} \quad \frac{\partial u}{\partial x} - \frac{\partial v}{\partial y} \equiv s_n \tag{7}$$

$$\text{shear strain} \quad \frac{\partial v}{\partial x} + \frac{\partial u}{\partial y} \equiv s_s \tag{8}$$

A purely rotational flow (vorticity) does not separate particles. Particle separation is controlled by the combined effect of divergence and nondivergent strain.[43] An eddy core is an "elliptic" regime where vorticity dominates over strain, and particle trapping and transport occurs. The core is surrounded by a hyperbolic regime where strain dominates over vorticity,[44] and filamentation and mixing occurs leading to dispersion.

4.4 LAGRANGIAN AND EULERIAN DIAGNOSTICS OF THE FLOW FIELD

There are numerous techniques to quantify dispersion and resolve coherent flow features in a horizontal velocity field (e.g., Refs 45–47). Some methods are based on Lagrangian, time-dependent information (e.g., Lyapunov exponents), whereas others require only a Eulerian snapshot of the velocity field (e.g., Okubo-Weiss). In general, Lagrangian techniques are the preferred approach because they integrate in time, allowing resolution of coherent structures in the flow field; whereas Eulerian methods will resolve an instantaneous flow field that cannot distinguish between coherent and transient features. Advantages to the Eulerian approach when using

real data are the ease of calculation and retained spatial coverage. Several studies have shown the utility of the Eulerian strain and divergence field for measuring particle dispersion.[43,47,48]

Here we apply the Eulerian method, based on a consideration of the oceanography in the SOF; the strong FC advects flow patterns quickly through the domain. Techniques based on integration time that attempt to capture coherent features of the flow would suffer from either lack of data (because seeded particles quickly exit the region) or would have to drastically reduce the length of integration to retain spatial information, so would converge to near-instantaneous values.

An *instantaneous* rate of separation (IROS) is the Eulerian metric that determines how an infinitesimally small particle will be moved by an instantaneous velocity field, and it is equal to the finite-time Lyapunov exponent (FTLE) at time $t = 0$.[43] It can be calculated from the sum of divergence (d) and total strain (s_n and s_s). The FTLE picks out features that dominate over longer time periods, whereas IROS acts as a guide to how the particles react in the moment.[43] High values of IROS indicate regions of elevated particle dispersion.

4.5 EULERIAN VELOCITY FIELD DURING AN EDDY EVENT

The components of the velocity gradient tensor exhibited large magnitude changes during the eddy passage (Figure 6). In the absence of an eddy event, the vorticity structure is dominated by the FC shear; there is uniform positive vorticity to the west of the jet axis, switching to negative vorticity on the eastern side, with magnitudes close to f (Figure 6(c)). However, when the submesoscale frontal eddy moved through the domain, the vorticity showed strong nonuniform fluctuations in time and space (of both positive and negative sign) that approached $11f$. For this reason, the dynamics of the frontal eddy are clearly within the submesoscale because the Rossby number (vorticity normalized by f) is very large.[49]

The IROS field during the eddy passage was similarly complex with strong magnitudes that revealed regions with a strong dispersive nature. A comparison of IROS and vorticity reveals co-location of peak values, which indicates that regions of strong vorticity in eddy cores do not necessarily correspond to particle trapping in the FC. This is because the eddy core is not purely rotational, as deformation plays a significant role. During a quiescent period with no eddy activity, the IROS field comprised mostly low values across the domain (Figure 6(d)).

The field of maximum value (divergence and IROS) extracted from each period of interest (the eddy and no eddy cases) reveals the nature of the flow field (Figure 7). For the eddy passage, there is a clear "track" in which maximum values exceed background levels. There was strong divergence associated with the passage of the eddy, which peaked at $4f$ (Figure 7(a)). This is consistent with the pattern of SST discussed previously (Figure 5). IROS exhibits strong values during the event, implying that there is strong particle dispersion because of the presence of the eddy. Regions of strong divergence and IROS translate downstream with the eddy, which

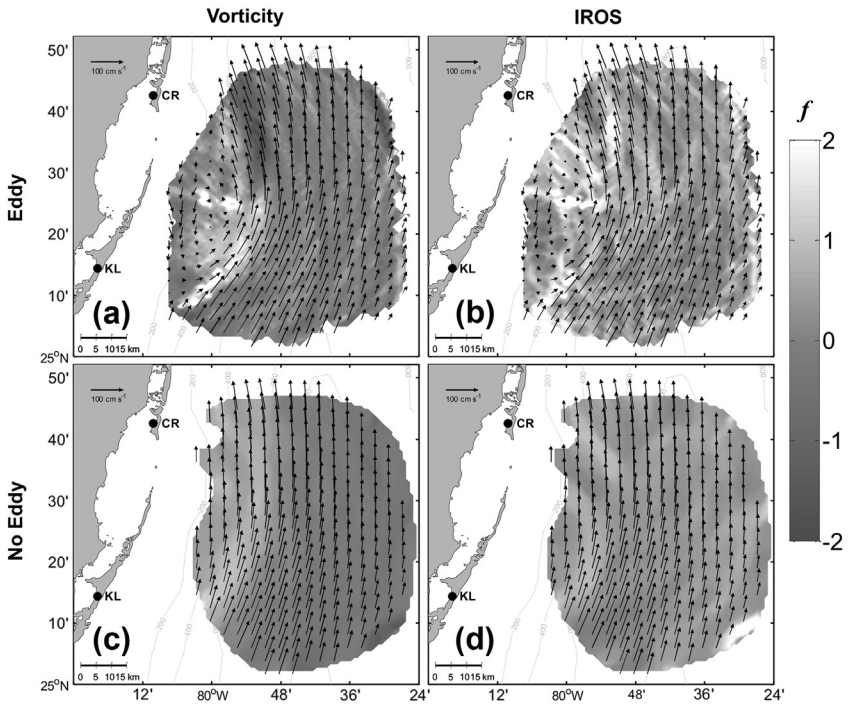

FIGURE 6

A snapshot of current vectors superimposed with fields of vorticity (a, c) and IROS (b, d) during an eddy event (January 20, 2005 at 16:00; a, b) and during a time with no eddy activity (October 4, 2006 at 00:00; c, d). The "no eddy" time period was identified as an example with relatively uniform downstream velocity, to contrast to the eddy event.

produces the track-like pattern in the maximum value field. When there is no eddy activity, the domain comprises small background levels, except along the periphery of the footprint where the GDOP is higher.

Velocity gradients during an eddy event exhibit very strong fluctuations in comparison to the FC flow field with no eddy activity. There was a complicated pattern of vorticity and deformation suggestive of strong particle leakage out of the eddy core, associated with high values of IROS. Divergence was strongly positive and consistent with concurrent MODIS SST imagery of cold water anomaly near the eddy core, associated with upwelling. These results indicate the energetic nature of these frontal eddies. Using the HF radar dataset to study the flux of kinetic energy between the mean and perturbations during both an eddy and no eddy period could shed light on the impact of eddies with respect to the energetics of the FC.

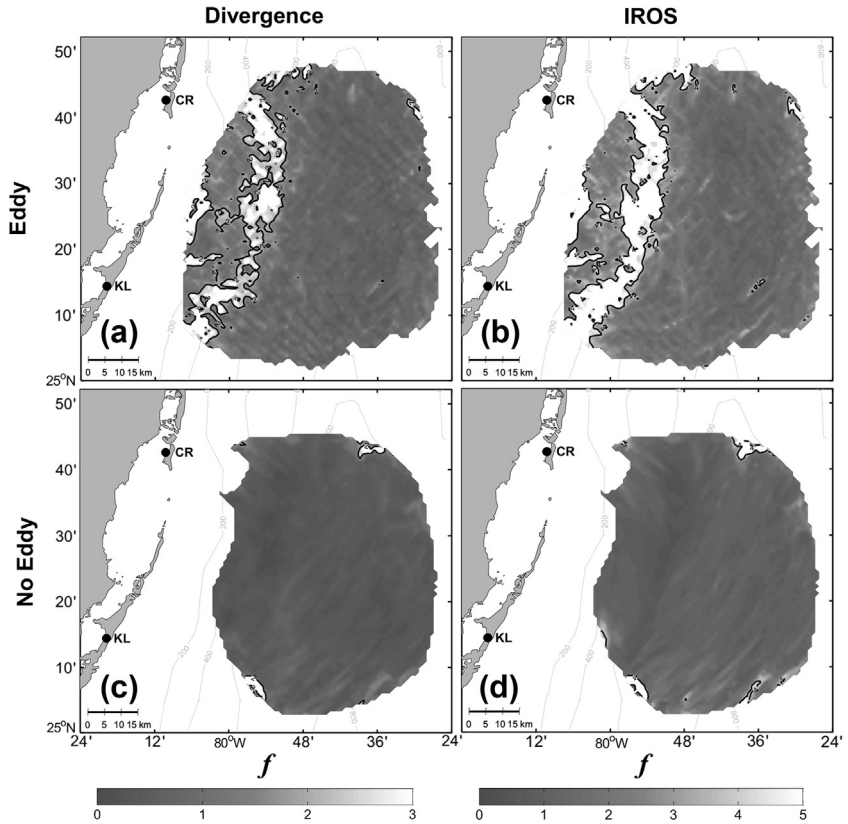

FIGURE 7

Maximum values of the field extracted for the time periods (a, b) 2005: 20 January 00:00 to 21 January 12:00 (eddy event) and (c, d) 2006: 3 October 12:00 to 4 October 16:00 (no eddy). Divergence is plotted with a $2f$ solid line contour (a, c) and IROS is plotted with a $4f$ solid line contour (b, d).

5. ANTICYCLONIC SHEAR-ZONE INSTABILITY

5.1 OBSERVED SURFACE CURRENT FIELD

Four consecutive eddy-like features were observed translating through the radar domain from 15 to 21 October, 2006. However, unlike the near-ubiquitous cyclonic frontal eddies observed along the western SOF, these features moved along the outer eastern flank of the FC. All four features exhibited clockwise rotation at the surface, in a water depth of approximately 650 m. The 19 October feature, which was best resolved in the radar footprint, is shown in Figure 8. This event produced a strong propagating signal in the time−longitude Hövmöller plot of u-component velocity (Figure 9(a)). The phase propagated northward at approximately 80 cm/s. By

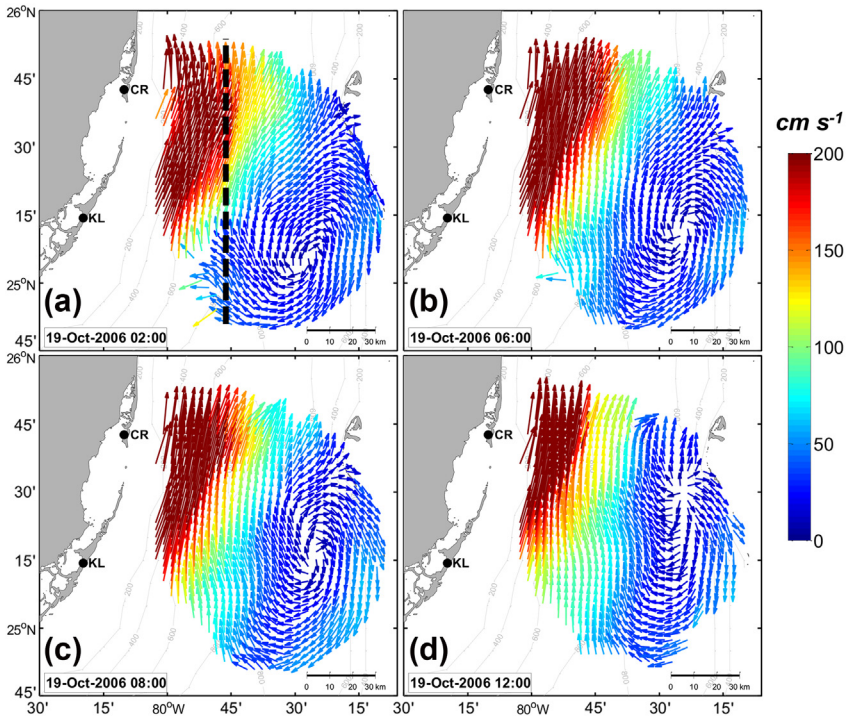

FIGURE 8

Four snapshots of the surface current vectors (hourly averaged) on 19 October 2006 at (a) 02:00 UTC, (b) 06:00 UTC, (C) 08:00 UTC and (d) 12:00 UTC reveal the evolution of a clockwise-rotating eddy observed by WERA HF radar. Dashed line in (a) depicts transect used for Hovmöller (Figure 9).

contrast, observed SOF cyclonic eddy translation speeds range between 6 and 19 cm/s (Tortugas eddies), 46−93 cm/s (frontal eddies), and 17−46 cm/s (submesoscale features).[8−10]

On 14 October, the wind speed increased from 5 to 12 m/s and shifted from a variable northerly wind to a steady easterly throughout the event. An easterly wind could force the currents shoreward (to the west), which was observed on 18 October, and may increase FC magnitude in the surface layer via wind-driven Ekman velocity. There was an observable increase in FC surface velocity at this time, peaking on 19 October (Figure 9(a)). However, because the disturbance was generated upstream of the observational domain, without additional data the contribution from the wind cannot be determined.

5.2 SEPARATING THE SIGNAL FROM THE BACKGROUND FLOW

The signal exhibited a periodicity close to the local inertial period ($2\pi f^{-1}$), which for latitudes from 25° to 25.7° ranges from 27.6 to 28.3 h. To separate from the

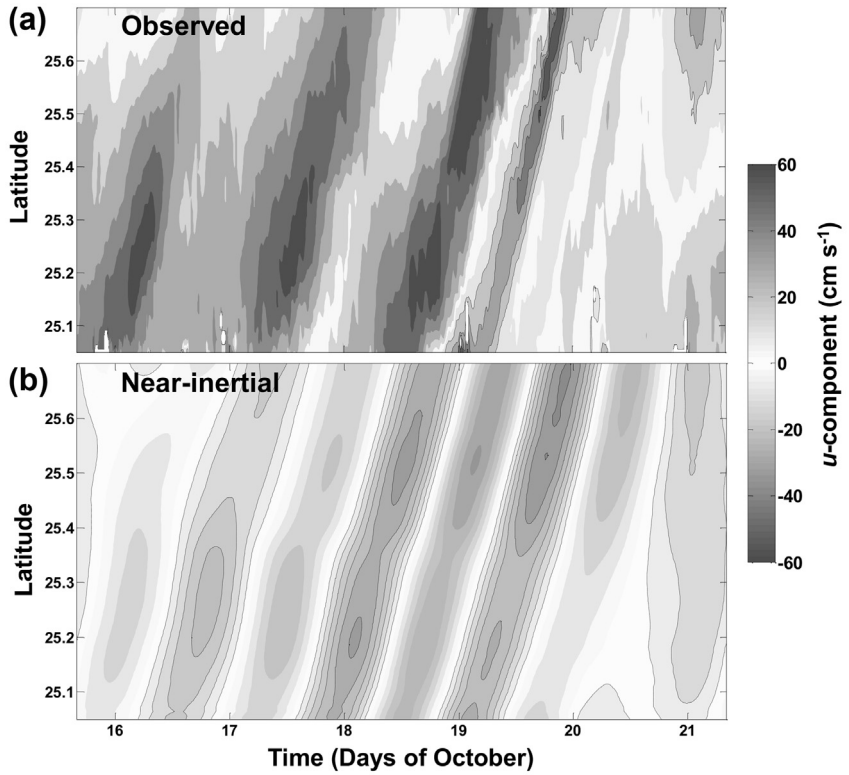

FIGURE 9

Hövmöller plots (u-component contours plotted on time vs latitude axes) at longitude 79.8°W (transect plotted in Figure 8(a)) for (a) observed and (b) near-inertial currents. Solid contour lines denote negative values. In (b), note the clear propagation of negative-u, which is masked out in the observed currents by the strong northward FC.

background flow (background is herein defined as the current field unassociated with the signal), the time series at each grid point was decomposed into subinertial (>48 h), near-inertial (20−36 h) and high frequency (<20 h) currents. The near-inertial bandwidth was assigned based upon the analysis of Mooers and Brooks,[6] who noted that because of the strongly sheared background flow, the inertial frequency can be shifted by up to 30% of f in the SOF. After conducting sensitivity tests, the Fourier filter proved optimal for the decomposition.[50] The Fourier filter requires a complete time series, which imposed restrictions on the spatial coverage of the dataset. The diminished spatial coverage does not fully cover the features that pass through (Figure 10(b)), although it does capture the rotation along the western periphery. This does not significantly affect the outcome; it can be shown that Reynolds decomposition, which uses all the data, gets the same qualitative result.

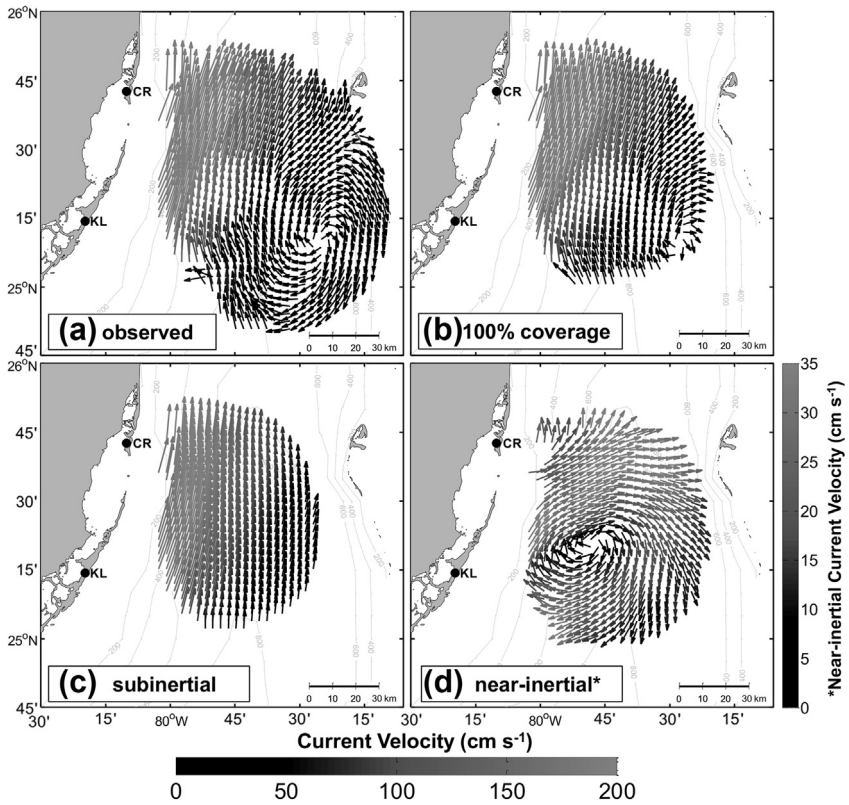

FIGURE 10

Frequency decomposition of the surface velocity field at 19 October 02:00 for (a) observed, (b) observed: region of 100% coverage that can be filtered, (c) subinertial, and (d) near-inertial components (*color bar scale for near-inertial currents is from 0 to 35 cm/s).

Tidal constituents were not removed because of the complication of contamination by the episodic FC meandering over daily time scales. Previous studies have shown that tidal velocities in the Straits are <10 cm/s.[1,51,52] Tidal forcing is continuous and periodic, whereas eddy events are transient and highly intermittent.

5.3 NEAR-INERTIAL OSCILLATION

The signal was embedded in the near-inertial band, as shown by decomposed surface current maps (Figure 10). The subinertial band comprised the FC meandering, whereas the high frequency band (not shown) exhibited neither coherent structure nor significant amplitude. Once isolated from the background flow field, the signal is oscillatory (Figure 9(b)). In the surface vector maps, the near-inertial currents reveal what can be interpreted as the crest and trough of a wave (Figure 11).

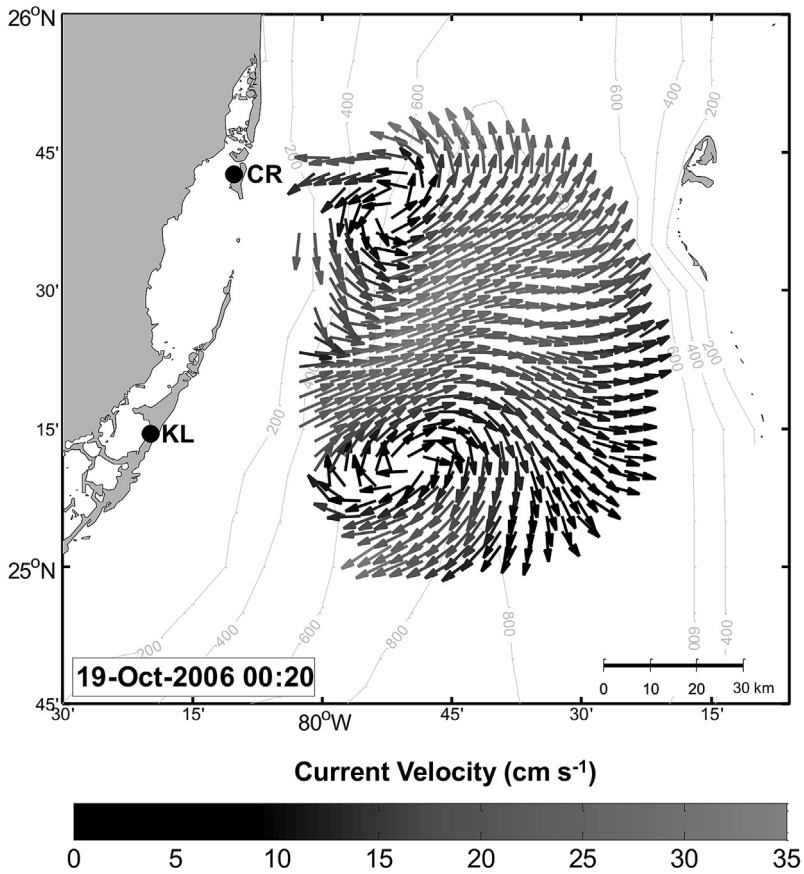

FIGURE 11

Near-inertial current vector map on 19 October 00:20 reveals the crest (convergence) and trough (divergence) of a near-inertial wave.

A clockwise rotation of the vectors in time produces horizontal convergence (crest) and divergence (trough) of the near-inertial currents.

Near-inertial motions can be generated by fluctuations in local wind stress,[53] or "loss of balance/spontaneous adjustment" by western boundary currents, mesoscale eddies, and submesoscale frontogenesis.[54–56] After a transient forcing event, and in the absence of all other forces, horizontal currents move under their own inertia, and on a rotating Earth in the Northern (Southern) Hemisphere will complete clockwise (counter-clockwise) oscillations at the inertial frequency f.[57] However, in the real ocean, these motions are often shifted off f because of other forces. A horizontal-sheared background flow, with relative vorticity ζ_g, can lower the bound of the internal waveband from f to an effective frequency $f_{eff} = f + \zeta_g/2$.[58] Kunze[59] showed

that when a near-inertial wave propagates through a horizontal gradient of f_{eff}, its wave vector must evolve to satisfy the dispersion relation, which leads to refraction and partial or total reflection. Horizontal gradients in f_{eff} result in a nonuniform wave field. Waves generated in regions where $f_{eff} < f$ are trapped, as they encounter turning points outside of the negative vorticity trough.[60] Elevated near-inertial kinetic energy on the anticyclonic (negative vorticity) side of a front has been observed in numerous field studies (e.g., Refs. 61–64).

Within the SOF, Shay et al.[10] documented near-inertial motions with horizontal wavelengths of 40 km that were trapped and advected by the FC. Vertical current structure measurements from an ADCP revealed vertical wavelengths between 50 and 100 m, and phase propagation reversals at a critical layer (the depth where the speed of the wave group equals that of the current).[59] Our case differs in that the near-inertial signal was observed in the anticyclonic shear-zone of the FC. The strongly sheared background flow partially masked the near-inertial current field, which is manifested as a succession of clockwise-rotating eddies in the observed surface current maps. The wave trough is not evident in the total surface currents when embedded in a laterally sheared flow regime. Some caution should be invoked, however, because this method filters Eulerian data to look at a translating Lagrangian feature. Further analysis must be conducted to relate this signal to near-inertial wave dynamics.

5.4 IDEALIZED MODEL

To elucidate the geometric effects of a background shear flow on the signal pattern observed in our HF radar domain, a simple analytical model of an asymmetric jet with lateral shear is superimposed with a dipole perturbation. Stream functions for the jet (ψ_J), perturbation (ψ_e), and total flow (ψ_T) are as follows:

$$\psi_J = A \cdot e^{-aL_x} \tag{9}$$

$$\psi_e = B \cdot \sin\left(m\pi^{-1}\right) \cdot \sin(l + \phi) \tag{10}$$

$$\psi_T = \psi_J + \psi_e \tag{11}$$

Where A is the amplitude of the jet core, a is a scaling factor for the lateral shear, and $L_x = L_y = 100$ are the zonal and meridional extent of the domain (size is arbitrary). B is the wave amplitude, $m = \pi/40$ is defined at $x = 10{:}50$ (where 40 is the width of the jet), $l = 2\pi/L_y$ is the meridional wave number, and ϕ the phase. The model has been assigned parameters to resemble the data: specifically, the wavelength/domain ratio and phase of the disturbance. The idealized fields are compared to the observations of the total surface currents, the band-passed near-inertial currents and the low-passed subinertial flow (Figure 12).

The model confirms that for a dipole perturbation embedded in a laterally sheared anticyclonic background flow, only closed clockwise rotation is apparent in the total flow field. The counter-clockwise rotating eddy acts to distort the stream function contours in the region (see the total fields in Figure 12), but there is no

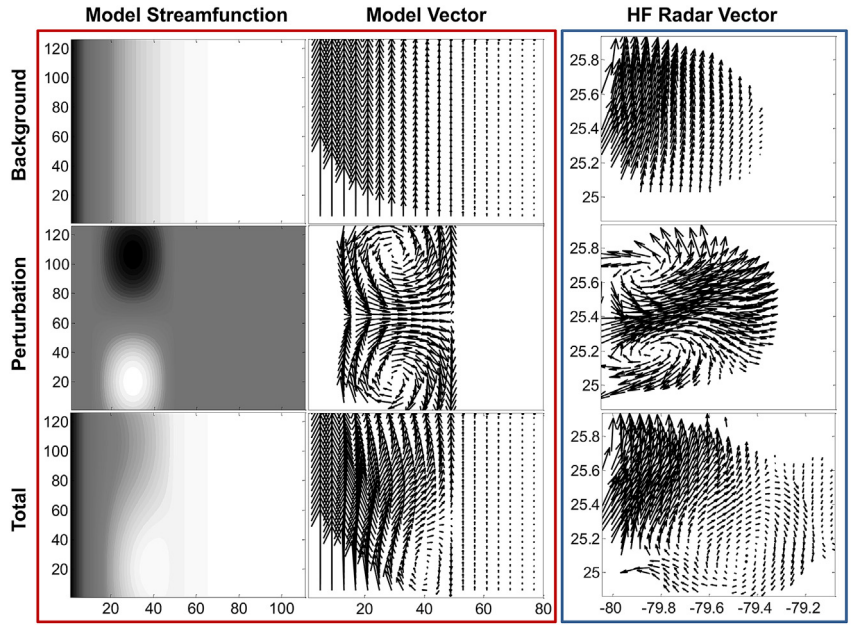

FIGURE 12

(left column) Model stream function, (middle column) model vector plots, and (right column) observed vector plots for (top) laterally sheared jet, (middle) dipole perturbation, and (bottom) total field.

closed circulation. Accounting for complications in the observed currents, such as differences in jet and eddy orientation, the simple model can replicate the basic flow pattern. This model reveals qualitatively how a horizontally sheared mean flow can mask a rotary perturbation signal.

5.5 NEAR-INERTIAL WAVE KINEMATICS

The hypothesis was that these transient clockwise-rotating features are a succession of stationary eddies advected northward by the FC. However, a systematic frequency analysis of the signal reveals these features to be strongly embedded in the near-inertial passband, and absent from the subinertial. The characteristics of the signal in frequency and space resemble a near-inertial oscillation. In this section, the properties of the signal are examined and compared to near-inertial wave theory.

5.6 SUBINERTIAL VELOCITY FIELD

The jet core was located in the western part of the radar domain, along the continental shelf. There was a thin region of cyclonic shear to the west of the axis and a much wider anticyclonic shear region to the east (Figure 10(c)). Within the core,

subinertial velocities (v) reached 200 cm/s, decreasing to less than 40 cm/s toward the east, over a distance (x) of 40 km. This equates to a sheared background flow with a normalized vorticity of $f^{-1}\ \partial v/\partial x = -0.6$. Similarly, the cyclonic shear-zone exhibited equal magnitudes in vorticity. This suggests that any near-inertial wave propagating in this field will experience strong horizontal gradients of f_{eff}, which could lead to frequency shifts and trapping in the negative vorticity trough.

5.7 WAVELENGTH

To determine the horizontal wavelength of the near-inertial signal, a series of trial wavenumbers ($2\pi/L$, where L is the wavelength) were fitted to the band-passed data at grid points along lines of constant longitude, using a plane wave model[10]:

$$u(y) = A_1 \cos(ly) + B_1 \sin(ly) + u_r(y) \tag{12}$$

$$v(y) = A_2 \cos(ly) + B_2 \sin(ly) + v_r(y) \tag{13}$$

where (u, v) are the observed near-inertial data, $A_{1,2}$ and $B_{1,2}$ are the velocity amplitudes (Fourier coefficients), l is the meridional wave number (trial wavelengths defined between 1 and 300 km), and (u_r, v_r) is the residual current not explained by the model. A "carrier" wave number is defined, which maximizes the correlation coefficient R between the observed and modeled data[65]:

$$R = \sqrt{\frac{\left(r_u^2 + r_v^2\right)}{2}} \tag{14}$$

where $(r_u,\ r_v) = s_{xy}^2/s_{xx}s_{yy}$, r_u and r_v are the correlation coefficients between observed and modeled velocity for the u- and v-components of velocity, s_{xx} and s_{yy} are the variance matrices of observed and modeled velocities, respectively, and s_{xy} is the covariance matrix. For each longitude, the latitudinal average was removed at each grid point in latitude, and the least squares fit was performed over two inertial periods (IP), the time period when the signal was at its strongest. Note: This approach assumes there is a dominant single carrier wave number for each longitude.

The model reveals an average wavelength of ~110 km (Figure 13). The wavelength is close to the Eady model most unstable mode of $3.9R_d$, where R_d is the Rossby radius of deformation, which in the SOF is ~30 km.[1]

5.8 FREQUENCY

The dominant frequency of the oscillation is calculated with Eqns (12) and (13) by substituting in frequency and temporal variations at each grid point in place of wave number and spatial variations. The near-inertial components at each grid point were fit to a series of trial frequencies between 0.5 and $1.5f$ (intervals of 0.05). The carrier frequency (2π/T, where T is the wave period) is defined as the value that maximizes the correlation between observed and modeled data,

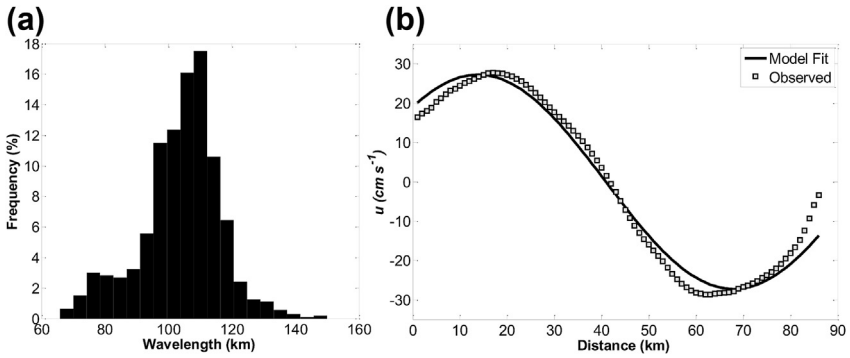

FIGURE 13

(a) Histogram of the modeled wavelengths between longitudes 79.5°W to 79.9°W and over a time period of 1.5 IP (43 hrs) and (b) results of least squares fit of the near-inertial currents at longitude 79.8°W.

over the two IPs. Over the domain, calculated carrier frequencies range between 0.8 and 1.3*f*, although a shifting to lower frequencies dominates, and the average is 0.87*f*, with correlations between the model and data as high as 0.95 (Figure 14). The width of the peaks is because of the broadband character of near-inertial motions.

5.9 EFFECTS OF SUBINERTIAL VORTICITY

The frequency shift of the signal below *f* agrees with theoretical results of a near-inertial wave propagating in a region of negative vorticity.[59] The mean near-inertial

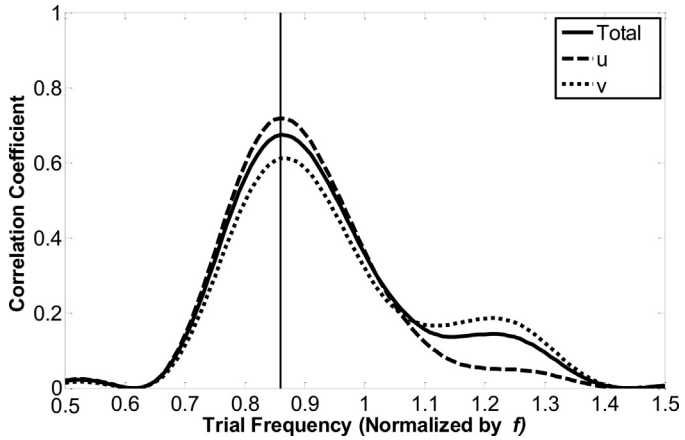

FIGURE 14

Trial frequency versus correlation between the model and data. Black vertical line denotes the carrier frequency, which has the best fit to the data.

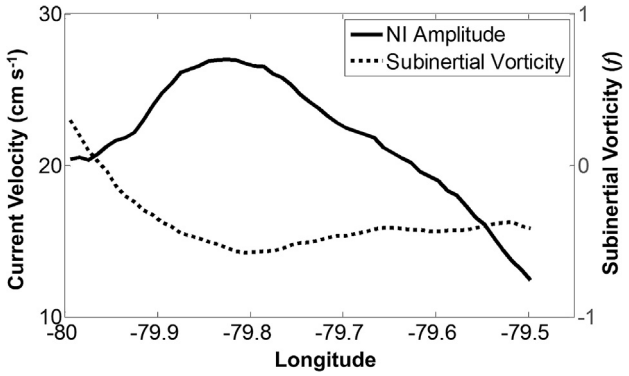

FIGURE 15

Near-inertial wave current amplitude associated with the dominant wavelength (solid) and the subinertial vorticity normalized by f (dashed), as a function of longitude over two inertial periods.

current amplitude distribution exhibits a peak aligned with the subinertial vorticity trough (Figure 15). This suggests trapping of the near-inertial signal generated in the vorticity trough. Trapping occurs because of wave refraction in a spatially nonuniform vorticity field—the wave cannot propagate freely away as it is refracted back and forth between regions of less negative vorticity, and it leads to peaks in near-inertial energy within the trough.[59,60]

5.10 OPEN QUESTIONS

The observed signal is consistent with near-inertial wave propagation in geostrophic shear.[59] The vector rotation at each grid point over most of the HF radar footprint is clockwise, which is consistent with near-inertial oscillations in the northern hemisphere. However, the rotation of vectors within the jet core and the strong cyclonic shear region is counter-clockwise (not shown). HF radar measures the Eulerian frequency $\omega = \omega_0 + \vec{k} \cdot \vec{V}$, where ω_0 is the intrinsic frequency, $\vec{k}$ is the wave vector, and $\vec{V}$ is the subinertial velocity. The Eulerian frequency is constant in a steady flow, but in our domain, it has a spatial gradient because of nonuniform f_{eff} and $\vec{V}$. The term $\vec{k} \cdot \vec{V}$ represents the Doppler shift (advection) by the background flow. In the North Atlantic subtropical zone, Mied et al.[66] found evidence of near-inertial waves strongly influenced by Doppler shifting. Preliminary results here indicate this Doppler shift may be significant enough to dominate the near-inertial oscillation frequency within the core. However, without additional observations, it is difficult to form a solid conclusion of the mechanism of the observed signal. One avenue for further insight could be to develop the idealized model by individually applying the dynamics of a vortex (e.g., a Rankine model) and a near-inertial wave. The

lateral shear and magnitude of the jet core can also be adjusted to best fit the observations. Because this study is the initial analysis of a new signal observed in the anticyclonic shear-zone of the FC, more observations of such events, covered by both remote and in situ instrumentation, as well as numerical modeling efforts, are required to fully explain these complex features.

6. SUMMARY

The deployment of HF radar along the South Florida coastline has improved our ability to monitor the ocean surface currents within the SOF. This has been shown by two case studies, which have demonstrated HF radar's ability to (1) examine how the flow field kinematics are significantly altered during the passage of a submesoscale frontal eddy, and (2) document a near-inertial velocity signal along the anticyclonic flank of the FC that has not been studied before.

In the first case study, the passage of a submesoscale cyclonic frontal eddy moving quickly downstream was captured in the HF radar footprint. In contrast to conditions recorded in a period of no eddy activity, during the event the vorticity field revealed a complex structure, with significant contributions from strain and a Rossby number that greatly exceeded unity, implying the flow field was governed by submesoscale dynamics. Indeed, there was strong horizontal current divergence near the core of the eddy, associated with anomalously cold water brought to the surface by upwelling, observed in MODIS SST satellite imagery. IROS, which is a metric of particle dispersion, exhibited high values that translated with the eddy, indicating the potential for strong dispersion of a passive tracer. This has important implications for cross-shelf exchange of water properties between offshore and coastal regions, and it is important information for SAR operations and pollution mitigation.

In the second case study, a transient, coherent signal in the near-inertial passband was identified. It was found that the strongly sheared FC partially masked the structure of the near-inertial oscillation, which was manifested as a succession of clockwise-rotating eddies in the observed surface currents. The wave trough was not evident when embedded in a laterally sheared northward background flow. The dominant frequency was shifted by $\sim 13\%$ below f in the average, which is consistent with a near-inertial wave propagating in a background regime with negative vorticity. The spatial pattern of frequency was highly anisotropic because of the variations in the subinertial current velocity and its associated vorticity. Near-inertial energy peaked in the negative vorticity trough along the FC's eastern flank, indicative of wave trapping in the horizontal. These results suggest the observed signal was governed by near-inertial wave dynamics. However, because this is a preliminary study of these features, further work is required to clarify their mechanisms.

These example cases, in addition to previous modeling and observational studies, reveal the highly intermittent nature of the flow within the SOF, which comprises periods of strong fluctuations on both the cyclonic and anticyclonic shear-zones of the FC. Future work needs to take the big step forward from individual case

studies to long-term time series analysis, which can determine the quantitative and statistical details of the time and space scales of these instabilities and whether they exhibit change over time. The ultimate goal is to incorporate this information into improving model forecasts of the current and wave field in the SOF.

ACKNOWLEDGMENTS

The authors gratefully acknowledge support by NOAA IOOS-supported South East Coastal Ocean Observing Regional Association (SECOORA) through grant NA11NOS0120033. We thank Pierre Flament, who suggested the comparison with an idealized model. Arthur Mariano, Rick Lumpkin, Ed Ryan, and Mitch Roffer contributed with productive discussions regarding data analysis. We are thankful for technical support from Jodi Brewster and Claire McCaskill. MODIS SST data was obtained from http://mur.jpl.nasa.gov/.

REFERENCES

1. Peters H, Shay LK, Mariano AJ, Cook TM. Current variability on a narrow shelf with large ambient vorticity. *J Geophys Res Oceans (1978–2012)* 2002;**107**(C8):2-1.
2. Leaman KD, Vertes PS, Atkinson LP, Lee TN, Hamilton P, Waddell E. Transport, potential vorticity, and current/temperature structure across Northwest Providence and Santaren Channels and the Florida Current off Cay Sal Bank. *J Geophys Res Oceans (1978–2012)* 1995;**100**(C5):8561–9.
3. Meinen CS, Baringer MO, Garcia RF. Florida Current transport variability: an analysis of annual and longer-period signals. *Deep Sea Res Part I: Oceanogr Res Pap* 2010; **57**(7):835–46.
4. Schott F, Düing W. Continental shelf waves in the Florida Straits. *J Phys Oceanogr* 1976; **6**(4):451–60.
5. Johns WE, Schott F. Meandering and transport variations of the Florida Current. *J Phys Oceanogr* 1987;**17**(8):1128–47.
6. Mooers CN, Brooks DA. Fluctuations in the Florida Current, summer 1970. *Deep Sea Res* 1977;**24**(5):399–425.
7. Lee TN, Williams E. Wind-forced transport fluctuations of the Florida Current. *J Phys Oceanogr* 1988;**18**(7):937–46.
8. Lee TN, Mayer DA. Low-frequency current variability and spin-off eddies along the shelf of southeast Florida. *J Mar Res* 1977;**35**:193–220.
9. Fratantoni PS, Lee TN, Podesta GP, Muller-Karger F. The influence of loop current perturbations on the formation and evolution of Tortugas eddies in the southern Straits of Florida. *J Geophys Res Oceans (1978–2012)* 1998;**103**(C11):24759–79.
10. Shay LK, Lee TN, Williams EJ, Graber HC, Rooth CG. Effects of low-frequency current variability on near-inertial submesoscale vortices. *J Geophys Res Oceans (1978–2012)* 1998;**103**(C9):18691–714.
11. Shay LK, Cook TM, Haus BK, Martinez J, Peters H, Mariano AJ, et al. VHF radar detects oceanic submesoscale vortex along Florida coast. *Eos, Trans Am Geophys Union* 2000;**81**(19):209–13.

12. Fiechter J, Mooers CN. Simulation of frontal eddies on the East Florida Shelf. *Geophys Res Lett* 2003;**30**(22).
13. Boudra DB, Bleck R, Schott F. A numerical model of instabilities in the Florida Current. *J Mar Res* 1988;**46**(4):715–51.
14. Parks AB, Shay LK, Johns WE, Martinez-Pedraja J, Gurgel KW. HF radar observations of small-scale surface current variability in the Straits of Florida. *J Geophys Res Oceans (1978–2012)* 2009;**114**(C8).
15. Lee TN, Rooth C, Williams E, McGowan M, Szmant AF, Clarke ME. Influence of Florida Current, gyres and wind-driven circulation on transport of larvae and recruitment in the Florida Keys coral reefs. *Cont Shelf Res* 1992;**12**(7):971–1002.
16. Sponaugle S, Lee T, Kourafalou V, Pinkard D. Florida Current frontal eddies and the settlement of coral reef fishes. *Limnol Oceanogr* 2005;**50**(4):1033.
17. Bane JM, Brooks DA. Gulf Stream meanders along the continental margin from the Florida Straits to Cape Hatteras. *Geophys Res Lett* 1979;**6**(4):280–2.
18. Schmitz Jr WJ, Richardson PL. On the sources of the Florida Current. *Deep Sea Res Part A. Oceanogr Res Pap* 1991;**38**:S379–409.
19. Lee TN, Leaman K, Williams E, Berger T, Atkinson L. Florida Current meanders and gyre formation in the southern Straits of Florida. *J Geophys Res Oceans (1978–2012)* 1995;**100**(C5):8607–20.
20. Lee TN. Florida Current spin-off eddies. *Deep Sea Res Oceanogr Abstract* 1975;**22**(11): 753–65. Elsevier.
21. Haus BK, Wang JD, Rivera J, Martinez-Pedraja J, Smith N. Remote radar measurement of shelf currents off Key Largo, Florida, USA. *Estuar Coast Shelf Sci* 2000;**51**(5): 553–69.
22. Lee TN, Atkinson LP, Legeckis R. Observations of a gulf stream frontal eddy on the Georgia continental shelf, April 1977. *Deep Sea Res Part A. Oceanogr Res Pap* 1981; **28**(4):347–78.
23. Brooks DA, Mooers CN. Wind-forced continental shelf waves in the Florida Current. *J Geophys Res* 1977;**82**(18):2569–76.
24. Chew F. The turning process in meandering currents: a case study. *J Phys Oceanogr* 1974;**4**(1):27–57.
25. Brooks IH, Niiler PP. Florida Current at Key West – summer 1972. *J Mar Res* 1975; **33**(1):83–92.
26. Davis KA, Leichter JJ, Hench JL, Monismith SG. Effects of western boundary current dynamics on the internal wave field of the Southeast Florida shelf. *J Geophys Res Oceans (1978–2012)* 2008;**113**(C9).
27. Soloviev AV, Luther ME, Weisberg RH. Energetic baroclinic super-tidal oscillations on the southeast Florida shelf. *Geophys Res Lett* 2003;**30**(9).
28. Winkel DP, Gregg MC, Sanford TB. Patterns of shear and turbulence across the Florida Current. *J Phys Oceanogr* 2002;**32**(11):3269–85.
29. Leichter JJ, Deane GB, Stokes MD. Spatial and temporal variability of internal wave forcing on a coral reef. *J Phys Oceanogr* 2005;**35**(11):1945–62.
30. Leichter JJ, Wing SR, Miller SL, Denny MW. Pulsed delivery of subthermocline water to Conch Reef (Florida Keys) by internal tidal bores. *Limnol Oceanogr* 1996;**41**(7): 1490–501.
31. Kundu PK. Generation of coastal inertial oscillations by time-varying wind. *J Phys Oceanogr* 1984;**14**(12):1901–13.

32. Peng G, Mooers CN, Graber HC. Coastal winds in south Florida. *J Appl Meteorol* 1999; **38**(12):1740−57.
33. Schott F, Lee TN, Zantopp R. Variability of structure and transport of the Florida Current in the period range of days to seasonal. *J Phys Oceanogr* 1988;**18**:1209−30.
34. Xue H, Bane Jr JM. A numerical investigation of the Gulf stream and its meanders in response to cold air outbreaks. *J Phys Oceanogr* 1997;**27**(12):2606−29.
35. Crombie DD. Doppler spectrum of sea echo at 13.56 MHz. *Nature* 1955;**175**:681−2.
36. Stewart RH, Joy JW. HF radio measurements of surface currents. *Deep Sea Res and Oceanogr Abstract* December 1974;**21**(12):1039−49. Elsevier.
37. Gurgel KW, Antonischki G, Essen HH, Schlick T. Wellen Radar (WERA): a new ground-wave HF radar for ocean remote sensing. *Coast Eng* 1999;**37**(3):219−34.
38. Gurgel KW. Shipborne measurement of surface current fields by HF radar. In: *OCEANS'94. Oceans Engineering for Today's Technology and Tomorrow's Preservation. Proceedings*, vol. 3. IEEE; 1994. p. III−23.
39. Haltiner GJ, Williams RT. *Numerical prediction and dynamic meteorology*, vol. 2. New York: Wiley; 1980.
40. Chapman RD, Shay LK, Graber HC, Edson JB, Karachintsev A, Trump CL, et al. On the accuracy of HF radar surface current measurements: intercomparisons with ship-based sensors. *J Geophys Res Oceans (1978−2012)* 1997;**102**(C8):18737−48.
41. Flament P, Armi L. The shear, convergence, and thermohaline structure of a front. *J Phys Oceanogr* 2000;**30**(1):51−66.
42. Saucier WJ. Horizontal deformation in atmospheric motion. *Trans Am Geophys Union* 1953;**34**:709−19.
43. Futch V. *The Lagrangian properties of the flow west of Oahu* [thesis]. Manoa: University of Hawaii; 2009.
44. McWilliams J. The emergence of isolated coherent vortices in turbulent flow. *J Fluid Mech* 1984;**146**:21−43.
45. d'Ovidio F, Isern-Fontanet J, López C, Hernández-García E, García-Ladona E. Comparison between Eulerian diagnostics and finite-size Lyapunov exponents computed from altimetry in the Algerian basin. *Deep Sea Res Part I: Oceanogr Res Pap* 2009;**56**(1):15−31.
46. Beron-Vera FJ, Olascoaga MJ, Goni GJ. Oceanic mesoscale eddies as revealed by Lagrangian coherent structures. *Geophys Res Lett* 2008;**35**(12).
47. Poje AC, Haza AC, Özgökmen TM, Magaldi MG, Garraffo ZD. Resolution dependent relative dispersion statistics in a hierarchy of ocean models. *Ocean Model* 2010;**31**(1):36−50.
48. Haza AC, Özgökmen TM, Griffa A, Molcard A, Poulain PM, Peggion G. Transport properties in small-scale coastal flows: relative dispersion from VHF radar measurements in the Gulf of La Spezia. *Ocean Dyn* 2010;**60**(4):861−82.
49. Thomas LN, Tandon A, Mahadevan A. Submesoscale processes and dynamics. *Ocean Model Eddying Regime* 2008:17−38.
50. Walters RA, Heston C. Removing tidal-period variations from time-series data using low-pass digital filters. *J Phys Oceanogr* 1982;**12**(1):112−5.
51. Kielmann J, Düing W. Tidal and sub-inertial fluctuations in the Florida Current. *J Phys Oceanogr* 1974;**4**(2):227−36.
52. Mayer DA, Leaman KD, Lee TN. Tidal motions in the Florida Current. *J Phys Oceanogr* 1984;**14**(10):1551−9.

53. D'Asaro EA. The energy flux from the wind to near-inertial motions in the surface mixed layer. *J Phys Oceanogr* 1985;**15**(8):1043–59.
54. Ford R. Gravity wave radiation from vortex trains in rotating shallow water. *J Fluid Mech* 1994;**281**:81–118.
55. D'Asaro E, Lee C, Rainville L, Harcourt R, Thomas L. Enhanced turbulence and energy dissipation at ocean fronts. *Science* 2011;**332**(6027):318–22.
56. Alford MH, Shcherbina AY, Gregg MC. Observations of near-inertial internal gravity waves radiating from a frontal jet. *J Phys Oceanogr* 2013;**43**(6):1225–39.
57. Cushman-Roisin B. *Introduction to geophysical fluid dynamics*. Englewood Cliffs, New Jersey: Prentice Hall; 1994.
58. Mooers CN. Several effects of a baroclinic current on the cross-stream propagation of inertial-internal waves. *Geophys Astrophys Fluid Dyn* 1975;**6**(3):245–75.
59. Kunze E. Near-inertial wave propagation in geostrophic shear. *J Phys Oceanogr* 1985; **15**(5):544–65.
60. Lee CM, Eriksen CC. Near-inertial internal wave interactions with mesoscale fronts: observations and models. *J Geophys Res Oceans (1978–2012)* 1997;**102**(C2):3237–53.
61. Kunze E, Sanford TB. Observations of near-inertial waves in a front. *J Phys Oceanogr* 1984;**14**(3):566–81.
62. Granata T, Wiggert J, Dickey T. Trapped near-inertial waves and enhanced chlorophyll distributions. *J Geophys Res Oceans (1978–2012)* 1995;**100**(C10):20793–804.
63. Rainville L, Pinkel R. Observations of energetic high-wavenumber internal waves in the Kuroshio. *J Phys Oceanogr* 2004;**34**(7):1495–505.
64. Nagai T, Tandon A, Yamazaki H, Doubell MJ, Gallager S. Direct observations of microscale turbulence and thermohaline structure in the Kuroshio front. *J Geophys Res Oceans (1978–2012)* 2012;**117**(C8).
65. Jaimes B, Shay LK. Near-inertial wave wake of hurricanes Katrina and Rita over mesoscale oceanic eddies. *J Phys Oceanogr* 2010;**40**(6):1320–37.
66. Mied RP, Lindemann GJ, Trump CL. Inertial wave dynamics in the North Atlantic subtropical zone. *J Geophys Res Oceans (1978–2012)* 1987;**92**(C12):13063–74.